



Influence of powder production process and properties on material properties of Ti6Al4V manufactured by L-PBF

Benjamin Meier^{1,2} · Fernando Warchomicka² · Jelena Petrusa¹ · Paul Angerer³ · Jaroslaw Wosik³ · Reinhard Kaindl¹ · Vojislav Petrovic¹ · Wolfgang Waldhauser¹ · Christof Sommitsch²

Received: 2 August 2022 / Accepted: 3 October 2022 / Published online: 15 October 2022
© The Author(s) 2022

Abstract

Besides process parameters, powder properties such as grain size, morphology, and chemical composition have the highest impact on the material properties of parts produced by powder-based additive manufacturing. These properties are strongly influenced by the production process of the powder and its feedstock. In the scope of this work, the influence of three different powder producers of Ti6Al4V, on density, chemical composition, and mechanical properties of build samples, is investigated. Furthermore, the effects of the varying atomization process on morphology, particle size distribution, chemical composition, and oxide layers are studied. Particle size distribution and flowability seem to have a minor influence on the production process while density depends highly on the surface topology, sphericity, and nature of the oxide layer, which affect energy intake. Tensile properties are highly influenced by chemical composition, mainly dissolved oxygen, and polluting satellites, while notched bar impact strength is additionally influenced by the oxide layer and suspected TiO₂ precipitations caused by it.

Keywords L-PBF · SLM · Ti6Al4V · Powder properties · Oxide layer · Powder production process

1 Introduction

With the fast expansion in powder-based additive manufacturing, different techniques of powder production are continuously developing to improve the quality of the powder and thus take an important place in the market. While standards for the chemical composition of Ti6Al4V (Ti64) are available (e.g., Ti64 Grade 5, Ti64 Grade 23), there is no comparable classification for the powder properties. Hence, the properties of the material processed by laser powder bed fusion (L-PBF) can vary and strongly influence the final product. For reactive materials like titanium and its alloys, different production processes are common to create a spherical powder: gas atomization (GA), plasma atomization (PA), and

plasma rotating electrode process (PREP) [1]. To achieve the particle size distribution (PSD) from 15 to 50 μm required in L-PBF, variants of GA and PA are state of the art nowadays since PREP is better suited for larger PSD. Other processes, like water and mechanical atomization, lack sphericity and chemical properties [1, 2].

There are several different gas atomization processes (Fig. 1 a-c), but in all of them, in the first step, the base material is molten. This can happen in various ways and therefore the material source is variable from bulk, rods to wires. A stream of mold then passes a nozzle system where high-pressurized gas is injected and atomizes the mold by creating a powder spray. For titanium and its alloys, either argon or helium is used. The advantages of this process are the wide selection of feedstock, the high throughput, and a less complex process, partly because melting and atomizing are separated. However, sphericity and control over output PSD are usually inferior compared to plasma atomization and further powder porosity, and the number of satellites is often higher. For free-fall gas atomization FFGA and close-coupled gas atomization CCGA, also contamination with ceramics from the containment is possible [1].

In plasma atomization (Fig. 1 d), melting and atomizing are done using plasma gas. Therefore, the material source is

✉ Benjamin Meier
benjamin.meier@joanneum.at; b.meier@student.tugraz.at

¹ Joanneum Research – Materials, Leobnerstraße 94,
8712 Niklasdorf, Austria

² IMAT Institute of Material Science, Joining and Forming,
University of Technology –Graz, Kopernikusgasse 24/1,
8010 Graz, Austria

³ MCL Material Center Leoben Forschung GmbH,
Roseggerstraße 12, 8700 Leoben, Austria

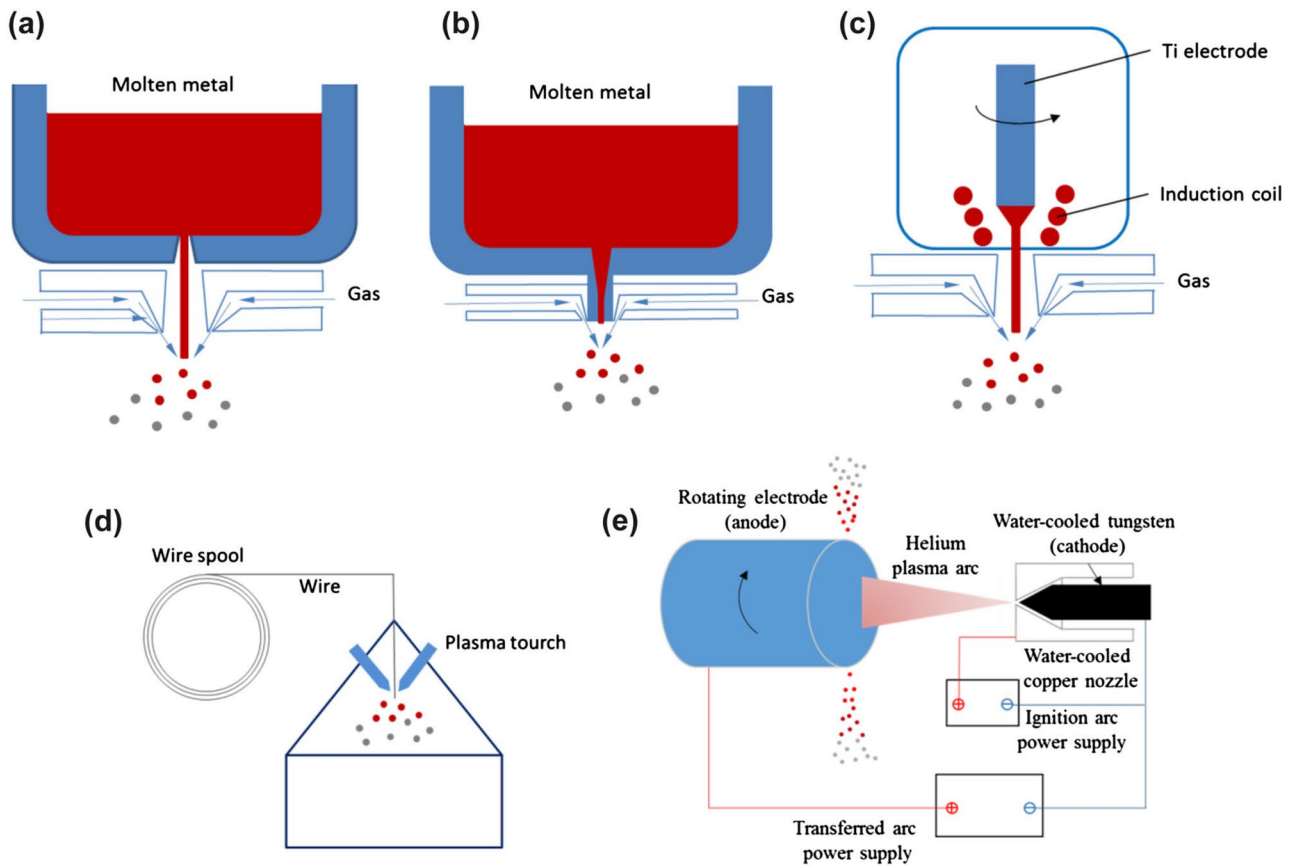


Fig. 1 Basic configuration of **a** free-fall gas atomization (FFGA), **b** close-coupled gas atomization (CCGA), **c** electrode-induction gas atomization (EIGA), and **d** plasma atomization (PA) and plasma rotating electrode process (PREP) [1]

limited, being either wire or a small diameter rod (or powder in case of plasma spheroidization PS). It is steadily injected into the plasma stream, molten, atomized, and solidified afterward. Sometimes, mechanical devices are included in the process to achieve even higher sphericity. As a drawback for most plasma atomizing processes, the powder has to be cleaned afterward. Furthermore, the limited types of feedstock, as well as lower material throughput, are a disadvantage. On the other side, plasma atomized powder shows superior sphericity, and the output in the grain size fraction of 20–60 μm , which is needed for L-PBF, is usually higher and better controllable than for other processes.

ASTM F3049 offers a standard for measuring properties with effect on additive manufacturing, but Sun et al. [3] show for Grade 5 powder used for electron beam melting, which calls for a larger PSD from 50 to 100 μm , that all properties, from PSD over sphericity to chemical composition, greatly vary between different powder providers. The same is indicated by Xie et al. [4] for titanium alloy Grade 23 and L-PFB, where powders from different providers and production processes show variation in particle size distribution, sphericity, and achieved ductility.

Therefore, we investigated the effects of different production processes and providers of Ti64 Grade 5 to understand the reasons that lead to different material properties, which are essential for critical technical components and applications.

2 Methodology

2.1 Powders

For this study, four Ti64 Grade 5 powder patches from three different manufacturers are investigated. In the following, these powders will be named A1, A2, B, and C; for an overview, see Table 1.

All build jobs are performed on an EOS EOSINT M280 equipped with a 400-W Nd:YAG Laser using virgin powder to prevent an influence of aging [5]. For all test specimens, the same parameters are used. After printing, the specimen received stress-relief heat treatment of 2 h at 650 $^{\circ}\text{C}$ in an argon-flooded Linn High Therm VMK-135 furnace.

Table 1 Powder patches

Power patch	Manufacturer	Claimed manufacturing Process	Remarks
A1	A	CCGA	Probably PA or PS
A2	A	CCGA	
B	B	PA	
C	C	PA	

2.2 Powder characterization

A first optical evaluation of the powders was performed on a Tescan Mira 2 scanning electron microscope (SEM). Evaluation of PDS and sphericity takes place in a CAMSIZER XT dynamic image analysis device according to ISO 13322–2. Flowability was tested using Hall and, if needed, a Carney flow meter.

The chemical composition of the powder was tested with the following methods: The oxygen and nitrogen content was determined by hot extraction in helium using a LECO TCH 600. Hydrogen concentration is measured using the inert gas fusion thermal conductivity method (JUWE H-Mat 2500 analyzer) and the argon by mass spectrometry (IPI ESD 100) while aluminum content was investigated by inductively coupled plasma optical emission spectrometry.

The oxide layer thickness in the particles was determined utilizing scanning electron microscopy (SEM). For this purpose, the embedded powder samples were subsequently cut by an ion slicer IM4000+ (Hitachi, Japan) in cross-section mode for 60 min at an excitation voltage of 6 kV. The SEM investigation was then conducted using a GeminiSEM®450 device (Carl Zeiss SMT, Germany) at an electron high tension (EHT) of 5 kV, a sample current of 3 nA, and a working distance of 8.6 mm. An AsB BSE detector was used to identify the oxide layer, while oxide concentrations were evaluated by a windowless EDX system (Ultim Extreme by Oxford Instruments, United Kingdom). Similar thin layer investigation is conducted by Motas et al. [6].

2.3 Density tests

Archimedes testing according to ASTM B962 was conducted on a Radwag PS 210 X2 digital scale to measure the density, using cubes with a side length of 15 mm printed with 20 different parameter sets. These 20 parameter sets were created within the DoE model. Each value is the mean value of 5 measurements.

2.4 Mechanical testing

For the characterization of mechanical properties, tensile and Charpy tests in different orientations (at least vertical and horizontal) were performed, the former ones on a Zwick and Roll universal test rig using cylindrical samples following ASTM 8 standards with a traverse speed of 1 mm/min and the latter using a 300-J Type PW30/15 Hammer and 10×10×55-mm specimen according to ISO standard. For tensile and Charpy tests, 5 specimens for each condition were tested at room temperature (Fig. 2).

3 Results and discussion

3.1 Rheology

SEM pictures of the powders (Fig. 3) give a first reference about the production process, sphericity, and pollution of the powder. The powder A1 shows the typical topology of gas atomization, namely a rougher, moon-like surface, and additional deformed particles but a very limited amount of satellites. Powders A2, B, and C seem to be plasma atomized. Plasma atomized powders typically offer close to perfect sphericity and smooth surfaces, sometimes covered with a larger number of satellites, which can be either of the base material, oxides, and/or other contaminations. However, this evaluation implies that powder A2 is not gas atomized as claimed by its manufacturer.

All powders are within recommended size for the L-PBF process between 15 and 60 μm (Table 2 and Fig. 4). While powder A1 and C show a little wider distribution (D10 of

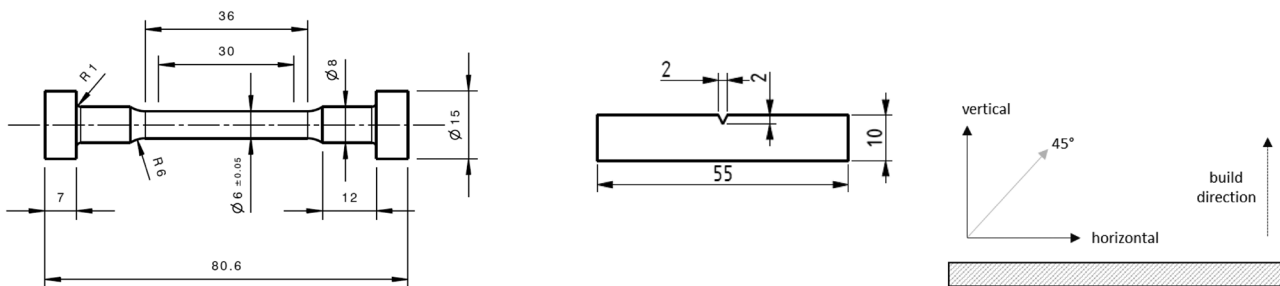
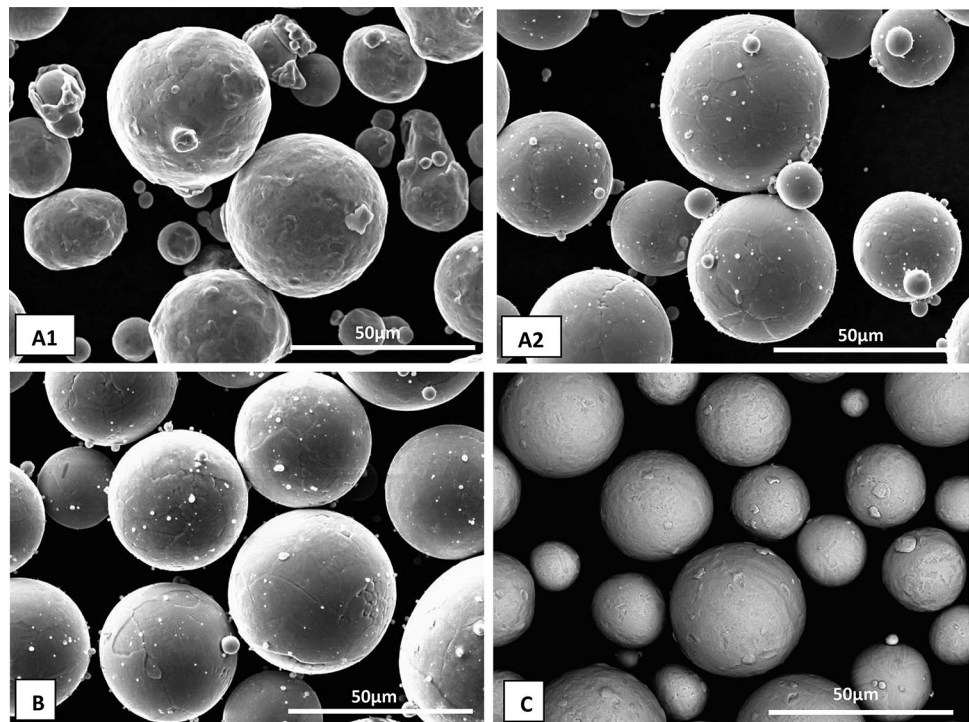


Fig. 2 Tensile (left) and Charpy (middle) specimen design and orientations (right)

Fig. 3 SEM investigation of the different powders



18.8 and 17.8 μm respectively), A2 and B are perfectly between 20 and 50 μm . For A1, the gas atomization process and therefore more irregular particles might explain the flatter distribution while manufacturer C claims that the powder placed at disposal was not sifted, which explains the larger fine fraction and an overall flatter curve. However, also this measurement shows that powder A2 is rather similar to power B than A. This wider span for GA powder can also be found in Xie et al. [4].

Sphericity measurements depicted in Table 2 confirm the observation made in SEM. Powder A got the lowest value for B/I3 of 0.94 due to the deformed particles and craters on the surface while plasma atomized powder C shows the best result at 0.98 followed by A2 with 0.97. SPHT3 sphericity for A is the lowest value at 0.89 while B, A2, and C are 0.93, 0.95, and C 0.97, respectively. The lower sphericity of powder B can be explained by the increased number of satellites, while for powder A, distortion of particles and the rougher surface topology contribute to it. This is in contrast with Xie et al. [4] who got similar sphericity for GA powder (0.94) but lower for PA powders (0.94 and even 0.87 for PS), which

either indicates a large difference in production patches or an inability by the manufacturer to make complete use of the advantages of the PA process.

3.2 Chemical powder properties

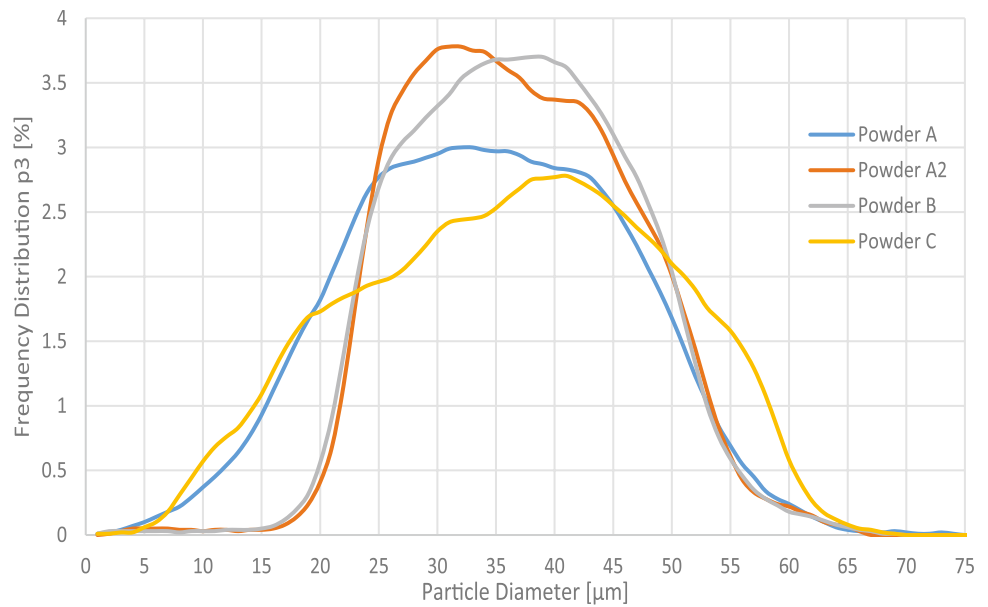
Table 3 shows the chemical composition of the powders and limits for Ti64 grade 5 found in ASTM B265. Powders A, A2, and B are well within those limits, especially the crucial oxygen, nitrogen, and hydrogen contents. Powders A2 and B reach oxygen levels close to the value for grade 23 specification of 0.13 at 0.14 wt.% [29]. Power C exceeds the limit of grade 5 by 0.03 wt.% which is due to already elevated values in the production feedstock as measured by the provider. Considering the O, N, and Al levels strengthens the suspicion of A2 being rather PA than GA powder, as plasma-optimized powders show nitrogen values below 0.017 wt.% rather than 0.028 for gas-atomized powder A. However, all are within the limit level of 0.05.

The higher amount of satellites found on powder B in SEM was analyzed using EDS (Fig. 5). It shows a high

Table 2 Particle size distribution, sphericity, and flow properties

Powder patch	D10 (μm)	D50 (μm)	D90 (μm)	Sphericity		Flow rate (s/50 g)
				SPHT3	B/I3	
A1	18.8	33.6	48.7	0.89	0.94	8.4 (Carney)
A2	23.9	34.9	47.9	0.95	0.97	10.5 (Carney)
B	24.6	36.5	48.8	0.93	0.95	8.9 (Carney)
C	17.8	36.4	52.8	0.97	0.98	

Fig. 4 Particle size distribution as frequency distribution for all powders



amount of oxide particles, which might be due to an inadequate passivation or cleaning process, which is required for most plasma atomization processes [1].

3.3 Oxide layer thickness

The levels of oxygen, hydrogen, and nitrogen are particularly important since they strongly influence mechanical properties (e.g., embrittlement due to oxygen) and therefore might even fail technical application [8]. Williams et al. [9] show the negative effect of oxide layers on particles of 0.4 and 0.7 wt.% on tensile strength and ductility.

In SEM observations at a magnification of 10,000, no oxide layers can be detected for powders A2 and B while C shows a layer of increased thickness (Fig. 6). Higher magnification at the surface of powder B (Fig. 7) shows an interrupted oxide layer added to the oxide particles shown in Fig. 5. Both oxygen and matrix titanium particles can be found using EDS.

Finally, high-resolution EDS measurements are performed on powders A2, B, and C in the oxide layer and the powder. The oxide layer was measured in three different positions: first, on what is supposed to be a pure oxide layer (darker coloration);

second, just inside of the oxide layer about 200 nm inside the layer; and finally, around 1 µm from the surface. All measurements were repeated on multiple powder particles. Finally, two more zone spectrums inside the particle were acquired for comparison, approximately in the middle and within the outer 10 µm of the particle respectively. Figure 8 shows examples of measurement points in the layer and close to it for powder A2, B, and C and the inside spectrums for powder B.

The chemical components measured in atomic % are shown in Table 4. However, measurements for light elements such as oxygen have to be taken with care, but relative changes in composition can be shown. Powder A2 shows no variation of oxygen at the surface and within the particle. Layers of powders B and C have increased oxygen levels, by 1–4% and 4–10%, respectively. For powder C, an increase in oxygen can also be observed for the area inside close to the oxide layer. Furthermore, the Al content increased for powders B and C in the layer with a decrease of V and Ti. The Al content measured in powder C is above the maximum dissolvable rate in α-Ti (~ 15 at.% [7]), and it indicates the presence of aluminum oxide Al₂O₃ or titanium aluminide. Comparative measurements inside the powders cross-section show stable chemical composition for all powders.

Table 3 Chemical composition measured by the methods mentioned in the methodology

Powder patch	Al (wt.%)	O (wt.%)	N (wt.%)	Ar (ppm)	H (ppm)
Powder A — GA	6.13	0.16	0.0281	1.1	21
Powder A2 — GA	6.36	0.14	0.0114	0.05	38
Powder B — PA	6.40	0.14	0.0071	0.11	14
Powder C — PA	5.73	0.23	0.017	1.7	19
Limits grade 5 [7]	5.50–6.50	Max. 0.20	Max. 0.05		Max. 125
Error	±0.34	±0.006	±0.00444		

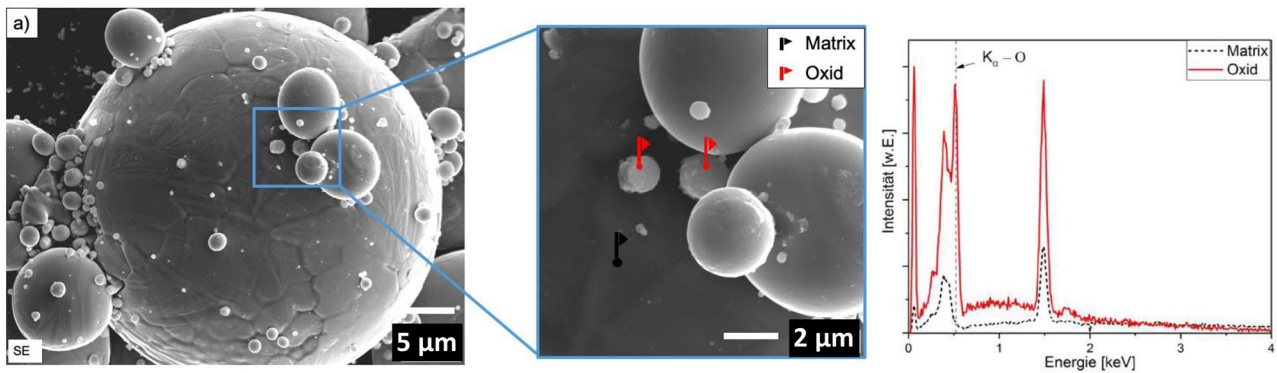


Fig. 5 Oxide particle pollution and satellites on powder B

Besides the influence of TiO_2 on mechanical properties, the varying optical and thermal properties are of interest for the L-PBF process. Since the powder particles are molten by the laser, absorption, reflection at the laser's wavelength, and surface topography have a great influence on process parameters and stability. Optical properties have a high influence on the particles' transition from solid to molten state, e.g., a large reflectance and low absorption ask for higher energy input. Thermal properties influence the melt pool as well as heat transport to the surrounding powder particles and therefore cooling rates, residual stresses, distortion, and crack forming.

Table 5 shows the optical properties for both, the involved oxides in the layer and the components of the metal matrix, for a wavelength of 1064 nm which matches that of the Nd:YAG laser used. Values from different literature may vary, but distinctive tendencies can be seen.

For the matrix Ti64, the material properties of Ti are most relevant since it makes up over 80 wt.% of the matrix. It shows a reflectance of 0.61504 at 0° and an absorption coefficient size of 10^5 . Taking this to the process level, it means when the laser beam hits a particle, more than half of the energy is reflected in an unmolten state. For the other alloy components, V shows similar optical properties as Ti while Al has higher values of reflectance at 0.9 and an absorption coefficient of 10^{10} .

Concerning components of the oxide layer, thin films of TiO_2 show a very limited reflectance at around 0.14 and high transmittance (0.7) while no absorption can be found ($\alpha=0$).

Al_2O_3 shows very different results concerning the sources, but in cases with an experimental setup that is most relevant for the L-PBF process, the reflectance is even lower than TiO_2 (0.06), and some absorption can be observed.

In Table 6, the thermal properties of the components involved are shown. The influence of both, optical and thermal properties, can be seen in L-PBF because the process parameters for aluminum alloys need higher energy input than titanium alloys. After all, aluminum has a higher reflectance of 0.9 and more than 10 times higher thermal conductivity although the melt temperature of 660°C is distinctively lower.

3.4 Bulk material properties

3.4.1 Density

Figure 9 shows the relative density of printed samples for the 4 different powders and varying sets of process parameters, which were actually developed for a DoE for powder A. Set 11 represents the standard set of parameters used for Ti64 at Joanneum Research. Powders A2 and C show the best average results over all parameters and, together with A, also the highest density for the parameter set 11, while B has the lowest values for both. The relative density for the parameter set 11 and average values of all parameter sets for all the studied powders can be found in Table 7.

Gas-atomized powder A shows a significant drop for parameter sets with lower energy density (Fig. 10), whereas

Fig. 6 Surface oxide layers of powder **A2** (left), **B** (middle), and **C** (right) at a magnification of 10,000

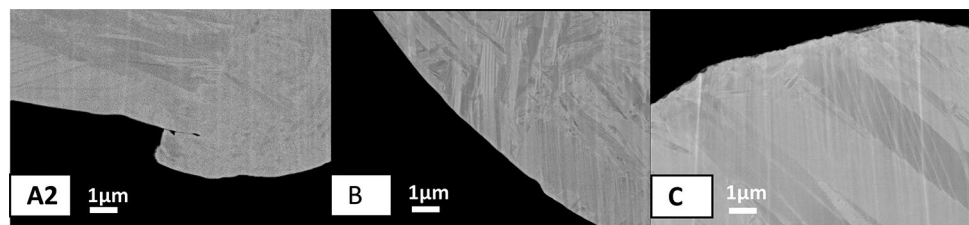
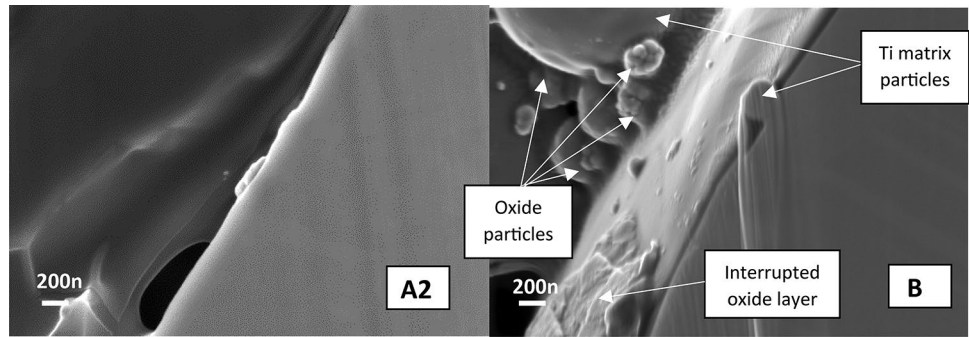


Fig. 7 Surface of powder **A2** and **B** at a magnification of 30,000



powder C seems to be mostly independent of the process parameters. Powders A2 and C are similar with C achieving slightly higher densities for lower energy input, which might be an effect of the larger fine-grained powder content.

Taking into account the sphericity and oxide layer measurements, the powder’s overall best density has the highest sphericity even though an oxide layer is present while the second best powder A2 shows no oxide layer but also high sphericity. For parameters with lower energy densities, powder C shows better relative density while for higher energy input, A2 performs better. This can be explained by the fact that both, TiO_2 and Al_2O_3 , have a lower reflectance than Ti; hence, the energy intake of powder with its oxide layer is higher. Even though not measured, a very limited oxide layer might be also present in powder A, since the density distribution over the energy input is similar to A2; however, the sphericity is inferior, which will lead to a more uneven energy intake and reflectance.

Powder C shows intermediate sphericity and inferior overall density, which seems to be due to the oxide satellites (Figs. 3, 5, and 7). The higher melt temperatures might cause instability in the melt pool; additionally, the partial and interrupted oxide layer will cause an uneven energy intake.

3.4.2 Tensile strength

Tensile tests for the stress-relieved specimen show the highest mean tensile and yield strength for all positions for powder C (1221 and 1116 MPa), followed by A2 (1176 and 1104 MPa), A (1172 and 1057 MPa), and B (1171 and 1055 MPa), depicted in Fig. 11 and Table 8. Elongation at break behaves indirectly proportionally, with B 5.3, A 4.9, A2 4.7, and C just 2.7%. It has to be mentioned that for powder A2, no specimens in 45° orientation were tested, which are averagely closer to vertical results than horizontal. Therefore, the mean values for A2 are more influenced by the horizontal tensile behavior.

Fig. 8 Examples for EDS measurement zones

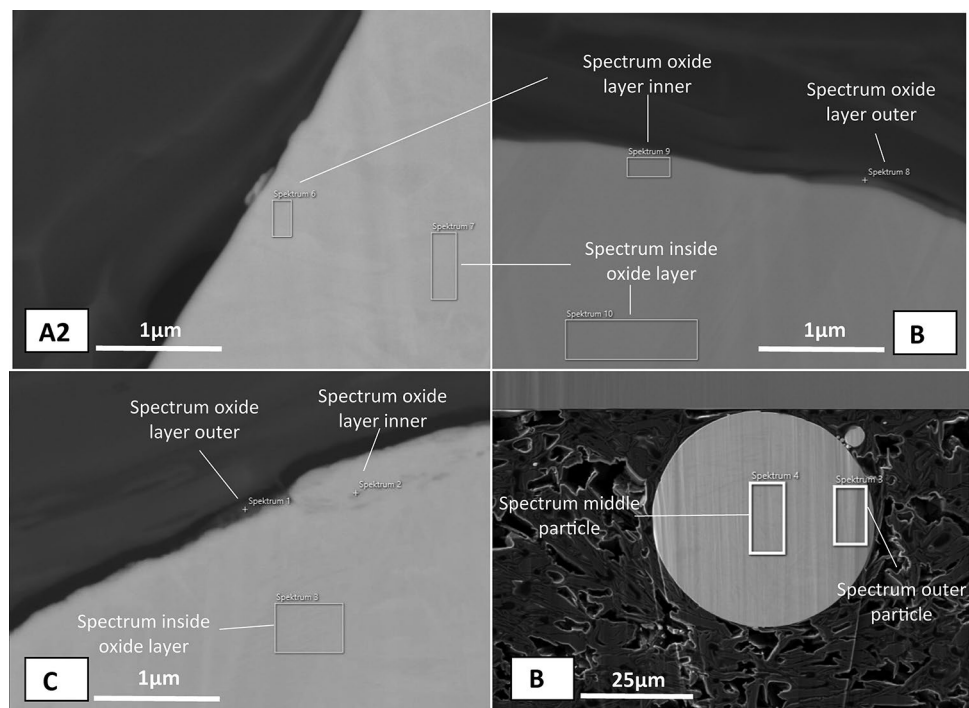


Table 4 EDS measurements for powders A2, B, and C in various locations

Powder	Location	O ₂	Al	Ti	V	O ₂ (overall, hot extraction)
		At. %	At. %	At. %	At. %	wt. %
A2	Oxide layer	5.25	8.16	85.12	1.48	0.14
	Oxide layer (inner)	4.78	7.68	85.24	2.29	
	Inside layer	4.26	7.77	85.85	2.13	
	Middle particle	4.83	7.75	85.10	2.33	
	Outer particle	5.00	8.01	85.35	1.64	
B	Oxide layer	8.02	12.23	79.73	0.01	0.14
	Oxide layer (inner)	4.52	8.09	85.26	2.03	
	Inside layer	3.7	8.1	85.79	2.41	
	Middle particle	4.17	8.23	85.97	1.68	
	Outer particle	4.41	8.23	85.67	1.68	
C	Oxide layer	8.25	34.68	54.93	1.6	0.23
	Oxide layer (inner)	13.4	8.67	77.34	0.6	
	Inside layer	3.81	7.23	89.93	2.33	
	Middle Particle	3.95	7.22	87.13	1.69	
	Outer particle	4.14	7.28	86.75	1.83	

Overall, the anisotropy for ultimate tensile strength is very limited (max. 22 MPa or 1.9% for powder B) whereas yield strength and elongation at break show a higher influence with orientation (Table 8). For powder B, an anisotropy of 141 MPa or 13.4% was measured for yield strength and 2.2% (total), respectively. This might not be only due to the elongated grain growth in the build direction [26] but also due to the increasing surface roughness from vertical to horizontal samples

since their surface is as-built and not machined. In addition, even though specimens received a stress-relief heat treatment, residual stresses are higher in horizontal samples due to larger exposure surfaces per layer [27, 28]. The tensile properties for powder A, A2, and B are in accordance with results found in the work of Liu and Shin [29] and Sun et al. [3] for stress-relief and as-built specimens from Ti6Al4V Grade 5. Powder C shows a brittle-breaking behavior with a decrease in elongation at

Table 5 Optical properties of oxides and metals**Optical coefficients for 1064 nm wavelength**

Material	Refractive index n	Extinction coefficient k	Absorption coefficient α	Transmittance	Reflectance	Type	Source
			1/cm	+ Fresnel losses, at 0°, in 0.1 μm layer			
TiO ₂	2.0718	0	0	0.77134	0.12174	Thin film 200 nm	[10]
	2.3078	0	0	0.7118	0.15632	Thin film 350 nm	[11]
	2.4789	–	–	–	0.18072	Crystal	[12]
Al ₂ O ₃	1.0818	9.1074	1.08E+06	5.24E–08	0.95042	Thin film, oxidized Al mirror	[13]
	1.6655	–	–	–	0.062342	Thin film	[14]
	1.6216	0.0001	6.53E+00	8.91E–01	0.056217	Thin film 497 nm, for 1539 nm	[15]
	1.726	0.0186	2196.8	0.84434	0.070972	Crystal	[13]
Ti	3.4654	4.0085	4.7342E+05	0.0013026	0.61504	Bulk	[16]
	2.9017	2.7503	3.25E+05	0.010078	0.49064	Bulk	[17]
	0.6470	9.1798	1.08E+10	1.73E–08	0.97025	Bulk	[18]
Al	1.0286	9.2524	1.09E+10	3.78E–08	0.95414	Bulk	[19]
V	2.8862	3.7154	4.39E+09	1.98E–03	0.60062	Bulk	[16]

Table 6 Thermal properties of oxides and metals

Thermal properties			
Material	Melting Point °C	Thermal conductivity Wm/K	Source
TiO ₂	1843	11.7	[20]
Al ₂ O ₃	2072	29.5	[21]
Ti	1668	17	[22]
Ti64	1660	7.2	[23]
Al	660	200	[24]
V	1910	30.7	[25]

break by nearly half compared to the other powders and necking of just 7 to 1.7%. This can be attributed to the higher overall oxygen level and exceeds even the tensile strength of highly oxidized powder by Williams et al. [9], indicating that the dissolved oxygen has more of an influence than TiO₂ layers and particles, as found on powder B. This goes in perfect line with Xie et al. [4], where also the powder with the higher oxygen content showed higher strength and less ductility, though not comparable in numbers since grade 23 specifications are different, and samples were furnace annealed.

3.4.3 Notched bar impact strength (Charpy)

Results of Charpy tests (Fig. 12) indicate the embrittlement due to oxygen content, or the presence of an increased amount of TiO₂, with falling impact energy from powder A2 (14.7 J–0.14 wt% O), B (13.9 J–0.14 wt% O), A1 (9.9 J–0.16 wt% O), and finally C (7.1 J–0.23 wt% O). The difference between powders A2 and B, which have the same overall oxygen pollution, can be explained by the surface particles and interrupted oxide layer seen on powder B and the resulting lower density of

Table 7 Relative density, average over all parameters (left), and for standard working parameters (right)

Powder	Average relative density — all sets of parameters	Relative density — standard parameters
A	99.5%	99.7%
A2	99.6%	99.8%
B	99.3%	99.5%
C	99.6%	99.7%

the samples. These oxides might build precipitations in the build specimen, leading to the found brittle dynamic break behavior.

In previous studies, Yasa et al. [30] show impact strength of 7 J for stress-relief heat treatment for 3 h at 595 °C, but without information about its chemical composition. Since their as-build samples without heat treatment performed better (11.5 J), oxygen pick up in heat treatment process might have happened since Lee et al. [31] are on a similar level with 7.3 J for stress-relieved specimens but just 6 J for as-build condition. However, information on oxygen levels is missing. Muiruri et al. [32] reach higher strength for not heat-treated specimen of about 14.4 ± 0.3 J but for Ti64 grade 23, with an oxygen level of just 0.082 wt.% but no heat treatment was performed. For the same alloy grade Monaheng et al. [33] achieve even values around 35 J but for stress-relieved and furnace-annealed specimens (650 °C for 3 h and 950 °C for 3 h, respectively), all performed in a vacuum furnace. Therefore, the oxygen level should not increase during heat treatment.

Thus, Charpy tests seem to be an adequate sensible and very economical way to evaluate the influence of oxygen levels and oxide layer thickness and therefore an indirect measure for powder quality.

Fig. 9 Relative density of all powders for different process parameters

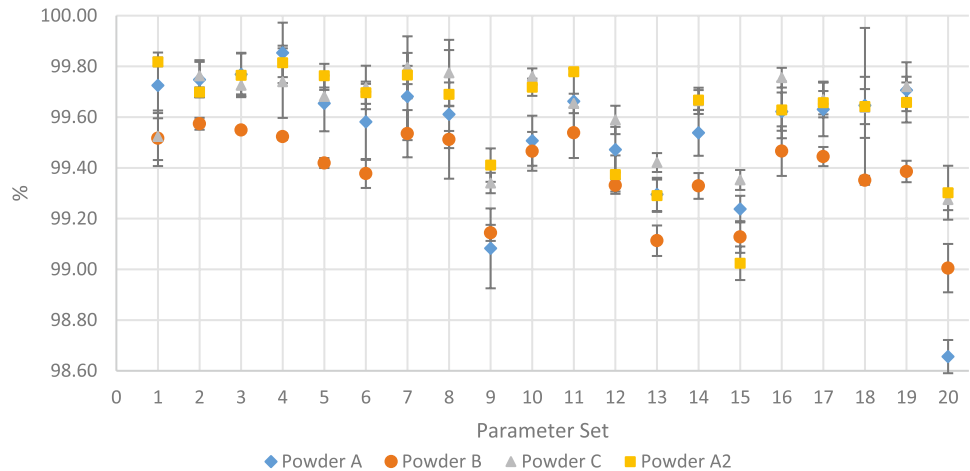


Fig. 10 Relative density vs. energy density of all powders

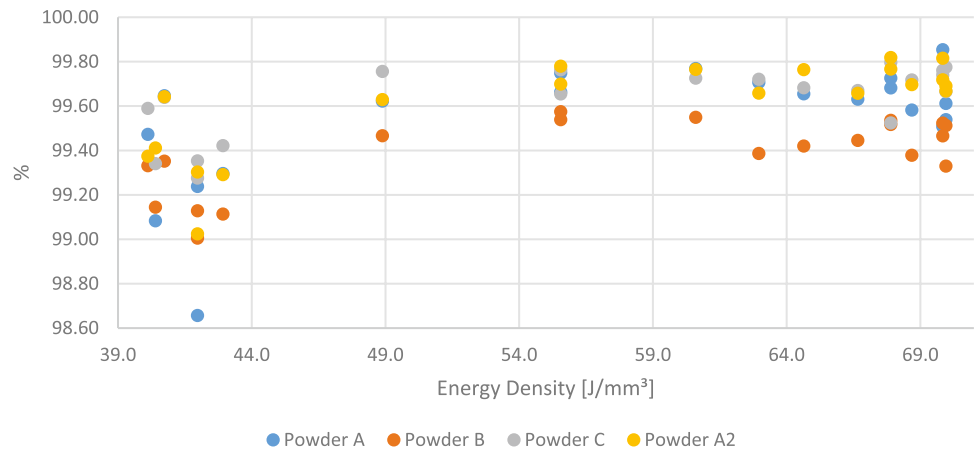


Fig. 11 Middle tensile properties for powders A, A2, B, and C in horizontal, vertical, and 45° orientation to the build plate

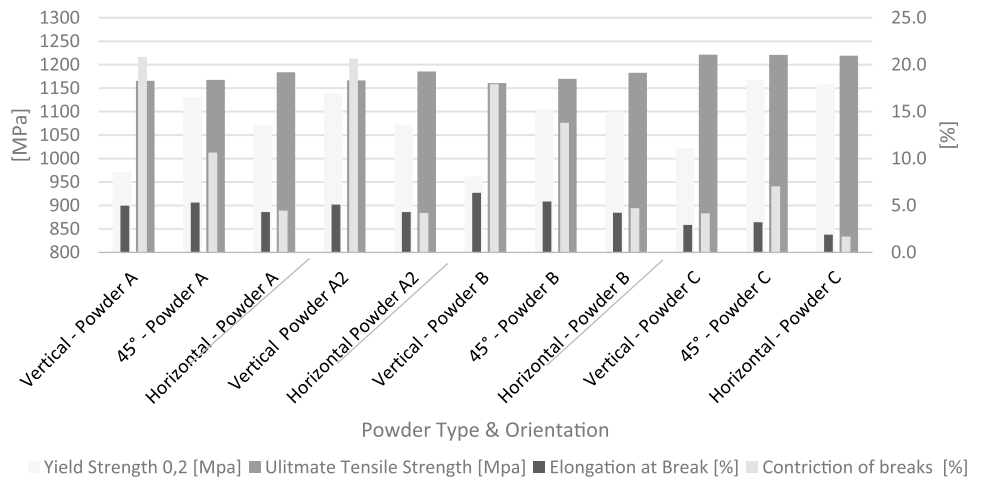
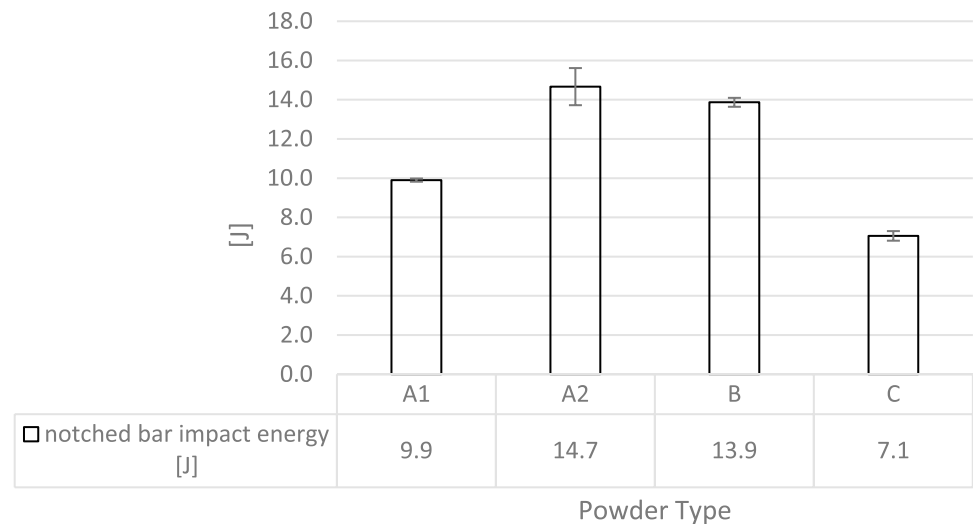


Table 8 Tensile properties, middle values, and deviation, $n=5$

Powder	Orientation	Yield Strength _{0,2}		Ultimate Tensile Strength		Elongation at Break		Constriction	
		Mpa	±	Mpa	±	%	±	%	±
A	Vertical	971	71	1166	10	5.0	1.6	20.8	11.3
	45°	1130	3	1168	3	5.3	0.1	10.6	2.8
	Horizontal	1072	38	1184	5	4.3	0.8	4.5	0.5
A2	Vertical	1138	17	1167	1	5.1	0.6	20.6	3.0
	Horizontal	1072	27	1186	3	4.3	0.6	4.2	0.4
B	Vertical	962	23	1161	27	6.4	0.5	17.9	0,0
	45°	1103	2	1170	5	5.4	0.5	13.8	4,0
	Horizontal	1100	17	1183	2	4.2	1.2	4.7	2,3
C	Vertical	1022	25	1221	21	2.9	1.1	4.1	1.2
	45°	1168	14	1221	3	3.2	0.2	7.0	0,0
	Horizontal	1158	6	1219	21	1.9	0.5	1.7	2,4

Fig. 12 Charpy test: notched bar impact energy — middle value: $n=5$ for all powders



4 Conclusions

Briefly, the properties of Ti64 components produced by L-PBF depend directly on the properties of the powder that is processed, based on the essential fact that appropriate process parameters are used. All of the delivered powders were processable by L-PBF.

Comparing results from chemical and physical powder analyses and density tests on the one hand and tensile and Charpy tests, on the other hand, leads to the conclusion that static mechanical properties are strongly influenced by the chemical composition and the formation of a stable oxide layer at the grain surface. Especially, increased oxygen content found in powder C leads to embrittlement. However, the proportionality is higher in Charpy tests while tensile test results are closer to each other, e.g., for powder A and A2. Considering oxide layer investigation, it seems that notched bar impact strength is massively influenced by the presence of TiO_2 and possibly even Al_2O_3 or intermetallic phases.

The density of build parts meanwhile seems to be mainly influenced by rheology and the chemical pollution on the surface of the powder, especially oxides and layers of them. While higher sphericity and tighter grain size distribution lead to a more even package and therefore stable melt pool, an uneven surface structure and residuals found on the surface influence laser reflection and energy absorption and therefore have a negative impact on the achieved density.

Concerning the tests done within this work, the influence of the difference in the PSD of the powders is negligible. However, all of them were within specification for L-PBF, with a flattened distribution for powder C and, to a lower extent, A1. It can be expected though that the larger proportion of the fine grain powder found in C will eventually diminish due to losses by the laminar flow and powder

handling. The upper size boundary is always met if sieving is executed appropriately to machines' standards.

Flowability has a strong impact on powder handling, and, varying with machine type, on recoating. In addition, issues with sieving and refilling can occur as well as an increased powder loss.

Therefore, knowledge about the powder, its production process, PDS and chemical composition, oxygen content, and the type of oxide layers covering the grains is essential to obtain stable and satisfying component properties.

Author contribution Conceptualization, B.M., F.W.; methodology, B.M., J.P., F.W., P.A., and V.P.; validation, F.W., R.K., and V.P.; formal analysis, B.M., F.W., C.B., A.S., and G.P.; investigation, B.M., F.W., J.P., P.A., and J.W.; resources, W.W. and C.S.; data curation, B.M., P.A., J.W., and J.P.; writing—original draft preparation, B.M., and F.W.; writing—review and editing, B.M., F.W., R.K., and P.A.; visualization, B.M. and F.W.; supervision, R.K., F.W., and C.S.; project administration, R.K. and V.P.; funding acquisition, R.K., V.P., and C.S. All the authors have read and agreed to the published version of the manuscript.

Funding Open access funding provided by JOANNEUM RESEARCH Forschungsgesellschaft mbH. This work was partially supported by the Federal Ministry Republic of Austria, Climate Action, Environment, Energy, Mobility, Innovation and Technology, Austrian Research Promotion Agency program Take-off, grant number 861050 and grant number 3859424. Additionally Supported by TU Graz Open Access Publishing Fund.

Data availability Data is contained within the article. If questions arise, additional information concerning data used in this study is available upon request from the corresponding author.

Code availability The software used is connected to the used equipment.

Declarations

Competing interests The authors declare no competing interests.

Open Access This article is licensed under a Creative Commons Attribution 4.0 International License, which permits use, sharing, adaptation, distribution and reproduction in any medium or format, as long as you give appropriate credit to the original author(s) and the source, provide a link to the Creative Commons licence, and indicate if changes were made. The images or other third party material in this article are included in the article's Creative Commons licence, unless indicated otherwise in a credit line to the material. If material is not included in the article's Creative Commons licence and your intended use is not permitted by statutory regulation or exceeds the permitted use, you will need to obtain permission directly from the copyright holder. To view a copy of this licence, visit <http://creativecommons.org/licenses/by/4.0/>.

References

- Sun P, Fang ZZ, Zhang Y, Xia Y (2017) Review of the methods for production of spherical Ti and TiAlloy powder. *Minerals Metals Mater Soc*. <https://doi.org/10.1007/s11837-017-2513->
- Irrinki H, Barmore B, Dexter M, Stitzel J, Badwe S, Pasebani S, Atre SV (2015) Effects of powder characteristics on the DMLS of 17–4PH stainless steel. *Conf Proc EuroPM2015*
- Sun Y, Aindow M, Hebert TJ (2018) Comparison of virgin Ti-6Al-4V powders for additive manufacturing. *ADDMA 285*
- Xie Bo, Fan Y, Zhao S (2021) Characterization of Ti6Al4V powders produced by different methods for selective laser melting. *Mater Res Express* 8:076510
- Meier B, Skalon M, Warchomicka F, Belei C, Görtler M, Kaindl R, Sommitsch C (2019) Effect of the reuse of powder on material properties of Ti6Al4V processed by SLM. *Proc 22nd Int ESAFORM Conf Mater Form ESAFORM*
- Motas JG, Gorji NE, Nedelcu D, Brabazon D, Quadrini F (2021) XPS, SEM, DSC and nanoindentation characterization of silver nanoparticle-coated biopolymer pellets. *Appl Sci* 11:7706. <https://doi.org/10.3390/app111167706>
- ASTM B265-20 (2020) Standard specification for titanium and titanium alloy strip, Sheet, and Plate
- Leyens C, Peters M (2003) *Titanium and titanium alloys*. Wiley-VCH Verlag; ISBN: 3–527–30534–3
- Williams R, Bilton M, Harrison N, Fox P (2021) The impact of oxidised powder particles on the microstructure and mechanical properties of Ti-6Al-4V processed by laser powder bed fusion. *ADDMA102181*
- Sarkar S, Gupta V, Kumar M, Schubert J, Probst PT, Joseph J, König TAF (2019) Hybridized guided-mode resonances via colloidal plasmonic self-assembled grating. *ACS Appl Mater Interfaces* 11:13752–13760
- Siefke T, Kroker S, Pfeiffer K, Puffky O, Dietrich K, Franta D, Ohlidal I, Szeghalmi A, Kley E-B, Tünnermann A (2016) Materials pushing the application limits of wire grid polarizers further into the deep ultraviolet spectral range. *Adv Opt Mater* 4:1780–1786
- Devore JR (1951) Refractive indices of rutile and sphalerite. *J Opt Soc Am* 41:416–419
- Querry MR (1985) Optical constants, Contractor Report CRDC-CR-85034
- Boidin R, Halenkovič T, Nazabal V, Beneš L, Němec P (2016) Pulsed laser deposited alumina thin films. *Ceram Int* 42:1177–1182
- Kischkat J, Peters S, Gruska B, Semtsiv M, Chashnikova M, Klinkmüller M, Fedosenko O, Machulik S, Aleksandrova A, Monastyrskiy G, Flores Y, Masselink WT (2012) Mid-infrared optical properties of thin films of aluminum oxide, titanium dioxide, silicon dioxide, aluminum nitride, and silicon nitride. *Appl Opt* 51:6789–6798
- Johnson PB, Christy RW (1974) Optical constants of transition metals: Ti, V, Cr, Mn, Fe Co, Ni, and Pd. *Phys Rev B* 9:5056–5070
- Palm KJ, Murray JB, Narayan TC, Munday JN (2018) Dynamic optical properties of metal hydrides. *ACS Photonics* 5:4677–4686
- Werner WSM, Glantschnig K, Ambrosch-Draxl C (2009) Optical constants and inelastic electron-scattering data for 17 elemental metals. *J Phys Chem Ref Data* 38:1013–1092
- McPeak KM, Jayanti SV, Kress SJP, Meyer S, Iotti S, Rossinelli A, Norris DJ (2015) Plasmonic films can easily be better: Rules and recipes. *ACS Photonics* 2:326–333
- <https://www.azom.com/article.aspx?ArticleID=1179> [Accessed 3 May 2022]
- <https://www.azom.com/article.aspx?ArticleID=3734> [Accessed 3 May 2022]
- <https://www.azom.com/article.aspx?ArticleID=9118> [Accessed 3 May 2022]
- <https://www.azom.com/properties.aspx?ArticleID=1547> [Accessed 3 May 2022]
- <https://www.azom.com/properties.aspx?ArticleID=1446> [Accessed 3 May 2022]
- <https://www.azom.com/article.aspx?ArticleID=9121> [Accessed 3 May 2022]
- Royer F, Bienvenu Y, Gaslain F (2015) EBSD observation of grains microstructures produced by selective laser melting. *Conf Proc Euro PM2015*
- DeRoy T, Wei HL, Zuback JS, Mukherejee T, Elmer JW, Milewski JO, Beese AM, Wilson-Heid A, De A, Zhang W (2018) Additive manufacturing of metallic components – process, structure and properties. *Prog Mater Sci* 92:112–224
- Malý M, Höller C, Skalon M, Meier B, Koutný D, Pichler R, Sommitsch C, Paloušek D (2019) Effect of process parameters and high-temperature preheating on residual stress and relative density of Ti6Al4V processed by selective laser melting. *Materials* 12(6):930
- Liu S, Shin YC (2018) Additive manufacturing of Ti6Al4V alloy: a review. *Jmade*
- Yasa E, Deckers J, Kruth J-P, Rombouts M, Luyten J (2009) Experimental investigation of Charpy impact tests on metallic SLM parts. *VRAP*
- Lee KA, Kim YK, Yu JH, Park SH, Kim MC (2017) Effect of heat treatment on microstructure and impact toughness of Ti-6Al-4V manufactured by selective laser melting; process. *Arch Metall Mater* 62:1341–1346
- Muiruri AM, Maringa M, du Preez WB, Masu LM (2019) Variation of impact toughness of as-built DMLS Ti6Al4V (ELI) specimens with temperature; *South African J Indust Eng* 29(3):Special Edition, pp 284–298
- Monaheng LF, du Preez WB, Polese C (2021) Towards qualification in the aviation industry: impact toughness of Ti6Al4V(ELI) specimens produced through laser powder bed fusion followed by two-stage heat treatment. *Metals* 11:1736. <https://doi.org/10.3390/met11111736>

Publisher's Note Springer Nature remains neutral with regard to jurisdictional claims in published maps and institutional affiliations.